Inverse Problems **25** (2009) 024003 (17pp) doi:10.1088/0266-5611/25/2/024003

Three-dimensional reconstruction from real data using a conjugate gradient-coupled dipole method

Patrick C Chaumet[1] **and Kamal Belkebir**

Institut Fresnel (UMR 6133), Université d'Aix-Marseille I and III, Av. Escadrille Normandie-Niemen, F-13397 Marseille cedex 20, France

E-mail: patrick.chaumet@fresnel.fr

Received 2 July 2008, in final form 22 December 2008
Published 6 February 2009
Online at stacks.iop.org/IP/25/024003

Abstract

The aim of the present work is to validate a full vectorial electromagnetic inverse scattering algorithm against experimental data. Data were provided courtesy of Institut Fresnel, Marseille, France. These data were carried out in an anechoic chamber and correspond to different canonical targets as well as one mysterious object which is known only by experimentalists who measured the associated scattered field. The inverse algorithm was first developed in the optical domain and is adapted herein to the microwave domain. It is an iterative approach where the parameter of interest, namely the relative permittivity distribution, is updated gradually by minimizing a cost function describing the discrepancy between data and those that would be obtained via a forward solver for the best available estimate of the relative permittivity. The forward solver is based on the coupled dipole method which was introduced in the seventies to study the scattering of light by non-spherical dielectric grains. The forward and inverse schemes are briefly described and various examples are presented that demonstrate the efficiency of the inverse algorithm.

(Some figures in this article are in colour only in the electronic version)

1. Introduction

The aim of inverse scattering problems is to determine geometrical and constitutive material features of unknown objects from the knowledge of their response to an exterior excitation. Applications of such problems cover the subsurface probing, non-destructive testing and imaging systems. Several authors have developed techniques for solving these nonlinear and ill-posed problems in one, two and three dimensions [1–4]. The most popular approach is to reconstruct parameters of interest iteratively. Starting from an

[1] To whom correspondence should be addressed.

initial guess, the unknown object is retrieved gradually by minimizing a cost function describing the discrepancy between measurements (data) and scattered fields computed via a forward solver for the best available estimation of the target under test. In this framework, the authors have developed three-dimensional inverse algorithms to image samples in the optical domain [5–9]. These algorithms were elaborated specifically for optical imaging systems such as microscopes where the goal is to retrieve a sample deposited on a substrate. Particular attention was paid to improving the resolution. For instance, in [7, 8, 10] a significant resolution was obtained with an internal reflexion illumination, i.e. samples to be imaged are illuminated with evanescent waves. This illumination can be realized with the use of a semi-spherical substrate. The resolution can even be drastically increased if one deposits the sample on a suitably designed grating [5, 11]. All these developments were achieved using synthetic data in the optical domain. One difficulty of using the aforementioned techniques is to measure the electromagnetic fields (modulus and phase) in the optical regime. There exist however interferometric devices that are able to measure the phase [12, 13]. We are presently studying this aspect of the optical imaging problem and unfortunately our inverse algorithms have not yet been tested against experimental optical data. Nevertheless, we have started to validate the inverse algorithm in the microwave domain [14] using canonical targets. The aim of the present work is to pursue the validation of our inverse algorithm against experimental data corresponding to various targets. The measured scattered fields were provided courtesy of Institut Fresnel, France.

2. Formulation of the forward scattering problem

The coupled dipole method (CDM) was introduced by Purcell and Pennypacker in 1973 for studying the scattering of light by non-spherical dielectric grains in homogeneous space [15] and is equivalent to a method of moment [16]. An overview of the CDM can be found in [17, 18]. The object under study is represented by a three-dimensional cubic array of N polarizable subunits. The local electric field at each subunit position is derived from the self-consistent equation:

$$\mathbf{E}(\mathbf{r}_i) = \mathbf{E}^{\mathrm{inc}}(\mathbf{r}_i) + \sum_{j=1,\, j\neq i}^{N} \mathbf{T}(\mathbf{r}_i, \mathbf{r}_j)\alpha(\mathbf{r}_j)\mathbf{E}(\mathbf{r}_j), \tag{1}$$

where $\mathbf{E}^{\mathrm{inc}}(\mathbf{r}_i)$ denotes the incident field at the position $\mathbf{r}_i$, i.e. the total electric field that would be observed in the absence of the scattering object. $\mathbf{T}$ describes the linear response of a dipole in homogeneous space [19, 20] and is expressed as

$$\mathbf{T}(\mathbf{r}, \mathbf{r}', \omega) = \mathrm{e}^{(\mathrm{i}k_0 R)} \left[\left(3\frac{\mathbf{R}\bigotimes\mathbf{R}}{R^2} - \mathbf{I} \right) \left(\frac{1}{R^3} - \frac{\mathrm{i}k_0}{R^2} \right) + \left(\mathbf{I} - \frac{\mathbf{R}\bigotimes\mathbf{R}}{R^2} \right) \frac{k_0^2}{R} \right]. \tag{2}$$

with $\mathbf{R} = \mathbf{r} - \mathbf{r}'$, k_0 being the wavenumber in vacuum and $\mathbf{I}$ the unit tensor. $\alpha(\mathbf{r}_j)$ is the polarizability of subunit j. According to the Clausius–Mossotti expression, the polarizability distribution α may be written as

$$\alpha(\mathbf{r}_j) = \frac{3d^3}{4\pi} \frac{\varepsilon(\mathbf{r}_j) - \varepsilon_0}{\varepsilon(\mathbf{r}_j) + 2\varepsilon_0}, \tag{3}$$

where d is the spacing of lattice discretization and $\varepsilon(\mathbf{r}_j)$ is the relative permittivity of the object. The relative permittivity of the homogeneous background medium is denoted by ε_0. There exist different prescriptions of the polarizabilities [21–24], but in the present study the expression of the polarizability corresponds to the weak form of the CDM [25, 26], and is accurate enough for the present study. In fact, with the weak form of the CDM we neglect

the radiative reaction term [27] which introduces in first approximation an additive term in the expression of the polarizability. This term depends on $\left(k_0^3 d^6\right)$, and as the spacing of lattice discretization is smaller than the wavelength of illumination, $(k_0 d)^3 \ll 1$. Hence, the addition of the radiative reaction term does not change the value of the polarizability. The error committed in the computation of the scattered field is small compared to the error in the measurements. However, in different topics, such as optical forces analysis [28–31] or the extinction cross-section modeling [32], taking into account the radiative reaction term is mandatory. The material under test is assumed to be isotropic. Hence, the relative permittivity $\varepsilon(\mathbf{r}_j)$ and subsequently the polarizability are both scalars.

Once the linear system represented by equation (1) is solved, the scattered field $\mathbf{E}^{\mathrm{d}}(\mathbf{r})$ at an arbitrary position $\mathbf{r}$ exterior to the object is given by

$$\mathbf{E}^{\mathrm{d}}(\mathbf{r}) = \sum_{j=1}^{N} \mathbf{T}(\mathbf{r}, \mathbf{r}_j)\alpha(\mathbf{r}_j)\mathbf{E}(\mathbf{r}_j). \tag{4}$$

The scattered field is collected at M observation points for L successive illuminations. Let the scattered field corresponding to the lth illumination with $l = 1, \ldots, L$ be $\mathbf{E}_l^{\mathrm{d}}$. For sake of simplicity, equations (1) and (4) are rewritten in a more condensed form:

$$\mathbf{E}_l = \mathbf{E}_l^{\mathrm{inc}} + \overline{\mathbf{A}}\mathbf{p}_l, \tag{5}$$

$$\mathbf{E}_l^{\mathrm{d}} = \overline{\mathbf{B}}\mathbf{p}_l, \tag{6}$$

where $\overline{\mathbf{A}}$ is a square matrix of size $(3N \times 3N)$ and contains all the field susceptibilities $\mathbf{T}(\mathbf{r}_i, \mathbf{r}_j)$. $\overline{\mathbf{B}}$ is a matrix of size $(3M \times 3N)$. The matrix $\overline{\mathbf{B}}$ contains the field susceptibilities, $\mathbf{T}(\mathbf{r}_k, \mathbf{r}_j)$, where $\mathbf{r}_j$ denotes a point in the discretized object, $j = 1, \ldots, N$, while $\mathbf{r}_k$ is an observation point, $k = 1, \ldots, M$. The vector $\mathbf{p}_l = \alpha\mathbf{E}_l$ represents the induced dipoles inside the scattering object for illumination l. Note that matrices $\overline{\mathbf{A}}$ and $\overline{\mathbf{B}}$ do not depend on the incident field nor on the object under test.

The local electric field at all lattice sites is found by solving iteratively the linear system represented by equation (5) using the quasi-minimal residual method of Freund and Nachtigal [33]. The computation of the local electric field can be accelerated by using the fact that the field-susceptibility tensor depends on the relative positions of the source point and the field point, rather than on their absolute locations. This means that $\mathbf{T}(\mathbf{r}_i, \mathbf{r}_j)$ can be written as $\mathbf{T}(\mathbf{r}_i - \mathbf{r}_j)$. This property of the field-susceptibility tensor allows equation (5) to be cast as a convolution product which can be computed efficiently using fast-Fourier transform (FFT) techniques [34–36]. Also, due to the property of the field-susceptibility tensor, the matrix $\overline{\mathbf{A}}$ is Toeplitz; hence, one needs to store only the first line of the matrix $\overline{\mathbf{A}}$ (one line for each component). Note that to use FFTs, we need to embed the Toeplitz matrix into a circulant matrix of a size twice larger than the size of the original one.

3. Formulation of the inverse scattering algorithm

Consider an unknown target, entirely confined in a bounded box $\Omega \subset \mathbb{R}^3$, successively illuminated by an $l = 1, \ldots, L$ electromagnetic plane wave. For each illumination l, the scattered field $\mathbf{\Psi}_l$ is measured on surface Γ. The inverse scattering problem consists in finding the complex relative permittivity ε distribution in Ω such that the corresponding scattering field $\mathbf{E}^{\mathrm{d}}$ matches the measured one $\mathbf{\Psi}$. This ill-posed nonlinear problem is solved iteratively. A sequence of polarizabilities $\{\alpha_n\}$ is constructed according to the following relation:

$$\alpha_n = \alpha_{n-1} + a_n d_n, \tag{7}$$

where α_n and α_{n-1} denote estimates of the unknown polarizability α for iteration steps n and $n-1$, respectively. d_n is an updating direction involving the gradient of the cost functional $\mathcal{F}(\alpha)$ with respect to α assuming that the internal fields $\mathbf{E}_l$ do not change. The scalar weight $a_n \in \mathbb{C}$ is determined by minimizing at each iteration step n the cost functional $\mathcal{F}_n$ defined as

$$\mathcal{F}_n(\alpha_n) = \frac{\sum_{l=1}^{L} ||\mathbf{\Psi}_l - \overline{\mathbf{B}}\alpha_n \mathbf{E}_{l,n}||_\Gamma^2}{\sum_{l=1}^{L} ||\mathbf{\Psi}_l||_\Gamma^2} = W_\Gamma \sum_{l=1}^{L} ||\mathbf{\Psi}_l - \overline{\mathbf{B}}\alpha_n \mathbf{E}_{l,n}||_\Gamma^2, \tag{8}$$

with $\mathbf{E}_{l,n}$ being the total electric field that would be present in Ω if the polarizability distribution was α_{n-1}. The field $\mathbf{E}_{l,n}$ is obtained by solving the dense linear system described by equation (1) with the polarizability taken equal to α_{n-1}. Substituting the expression of the polarizability α_n derived from equation (7) in equation (8) leads to a polynomial expression with respect to the scalar coefficient a_n. Thus, the minimization of the cost functional $\mathcal{F}_n$ is reduced to a minimization of a simple cost function $\mathcal{F}_n(a_n)$ for which the unique minimum is reached for

$$a_n = \frac{\sum_{l=1}^{L} \langle \overline{\mathbf{B}} d_n \mathbf{E}_{l,n} | \mathbf{\Psi}_l - \overline{\mathbf{B}}\alpha_{n-1}\mathbf{E}_{l,n}\rangle_\Gamma}{\sum_{l=1}^{L} ||\overline{\mathbf{B}} d_n \mathbf{E}_{l,n}||_\Gamma^2}, \tag{9}$$

where $\langle \cdot | \cdot \rangle_\Gamma$ denotes the inner product in L^2. As an updating direction d_n, we take the conjugate gradient direction

$$d_n = g_{n;\alpha} + \gamma_n d_{n-1}, \tag{10}$$

with $g_{n;\alpha}$ being the gradient of the cost functional $\mathcal{F}$ with respect to the polarizability assuming that the internal fields $\mathbf{E}_l$ do not change:

$$g_{n,\alpha} = -W_\Gamma \sum_{l=1}^{L} \mathbf{E}_{l,n}^* \cdot \overline{\mathbf{B}}^\dagger (\mathbf{\Psi}_l - \overline{\mathbf{B}}\alpha_{n-1}\mathbf{E}_l), \tag{11}$$

in which $\mathbf{u}^*$ represents the complex conjugate of $\mathbf{u}$ and $\overline{\mathbf{B}}^\dagger$ denotes the transpose complex conjugate matrix of the matrix $\overline{\mathbf{B}}$.

The scalar coefficient γ_n is defined as

$$\gamma_n = \frac{\langle g_{n;\alpha} - g_{n-1;\alpha} | g_{n;\alpha}\rangle_\Gamma}{||g_{n-1;\alpha}||_\Gamma^2}. \tag{12}$$

The initial guess of the iterative algorithm α_0 is estimated with a back-propagation procedure [7].

4. Numerical experiments

Results of the reconstruction of three-dimensional targets from experimental data are reported in this section. All data were provided courtesy of Institut Fresnel (Marseille, France). The parameters of the experimental set-up as well as the different objects under test will be described elsewhere in the present special section. This database is constituted of five dielectric targets of different shapes and sizes. The background medium is homogeneous $\varepsilon_0 = 1$. The first object is two cubes connected by a corner, the second one is two spheres in contact and the third one is an aggregate of 27 spheres. The fourth target is a cylinder and the last one is only known by the experimentalist who measured the scattered field. This target is referred to from now on as the mysterious target. All the presented results were obtained without any *a priori* information. Note that our inversion algorithm does not use any regularization technique.

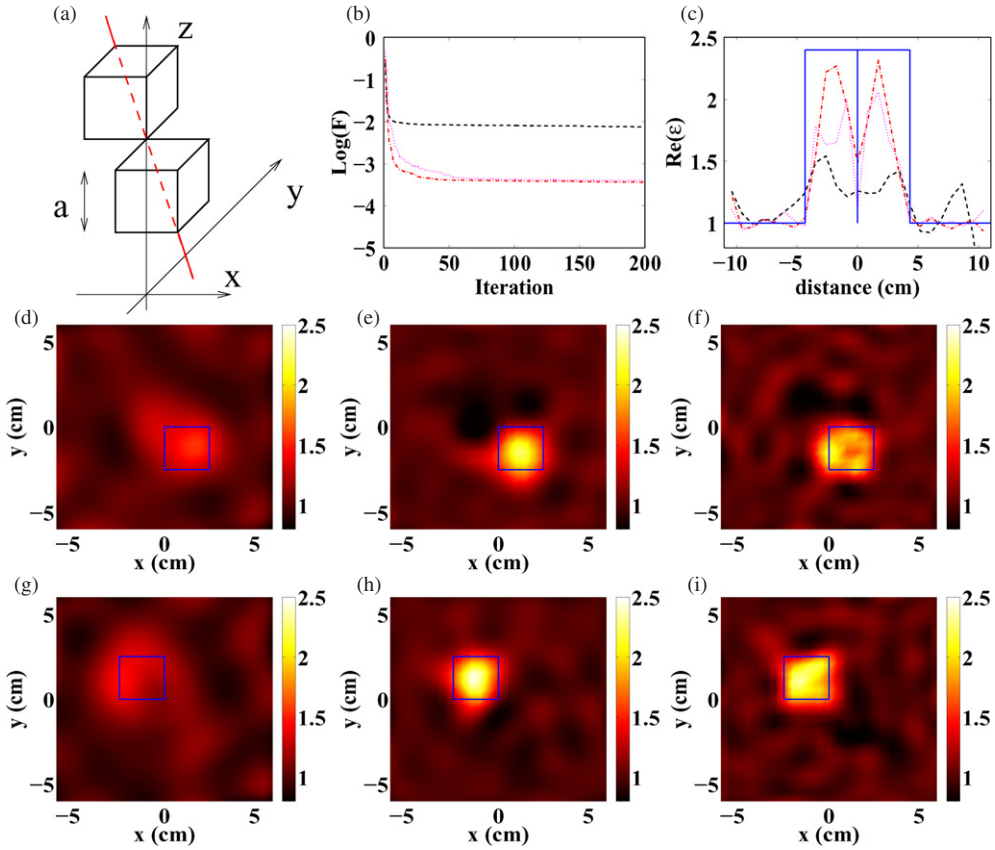

Figure 1. (a) Target under test: two cubes with relative permittivity $\varepsilon = 2.4$ and of side size $a = 2.5$ cm connected by a corner. Centers of cubes are located at $(-a/2, a/2, 3a/2)$ and $(a/2, -a/2, 5a/2)$. (b) Evolution of the minimized cost function in the log scale, 3 GHz (- -), 5 GHz (-·) and 7 GHz (· · ·). (c) Comparison between the reconstructed real part of the relative permittivity and the actual one along a line crossing the diagonals of the two cubes as well as the shared corner of the two cubes (as plotted in a dashed line in (a)) for 3 GHz (- -), 5 GHz (-·) and 7 GHz (· · ·). The full line is the actual profile. (d)–(f) are the map of the reconstructed relative permittivity in the (x, y) plane at $z = 3a/2$ for 3 GHz, 5 GHz and 7 GHz, respectively. (g)–(i) are the map of relative permittivity plotted in the (x, y) plane at $z = 5a/2$ for 3 GHz, 5 GHz and 7 GHz, respectively. The squares represent the boundaries of cubes.

For the inversion, the spacing lattice of the investigating domain Ω is $d = 5$ mm. The smallest wavelength of the illumination used in the numerical experiments is about $\lambda \approx 38$ mm and corresponds to the illumination at an operating frequency of 8 GHz. We kept this value of the spacing lattice fixed for all inversions, in particular for inversions at lower frequencies, hence ensuring accurate computation of the forward problem. The investigating domain Ω is a large cube of size $(125 \times 125 \times 125)$ mm^3. At the operating frequency of 8 GHz, the volume of the investigating domain Ω in terms of wavelength is about $36\,\lambda^3$. All final results reported correspond to the 200 th iteration. We did not note any marked changes in the results when continuing iterating. In addition, only the real part of the reconstructed permittivity is presented since the imaginary part remains very small in all cases. Furthermore, in all

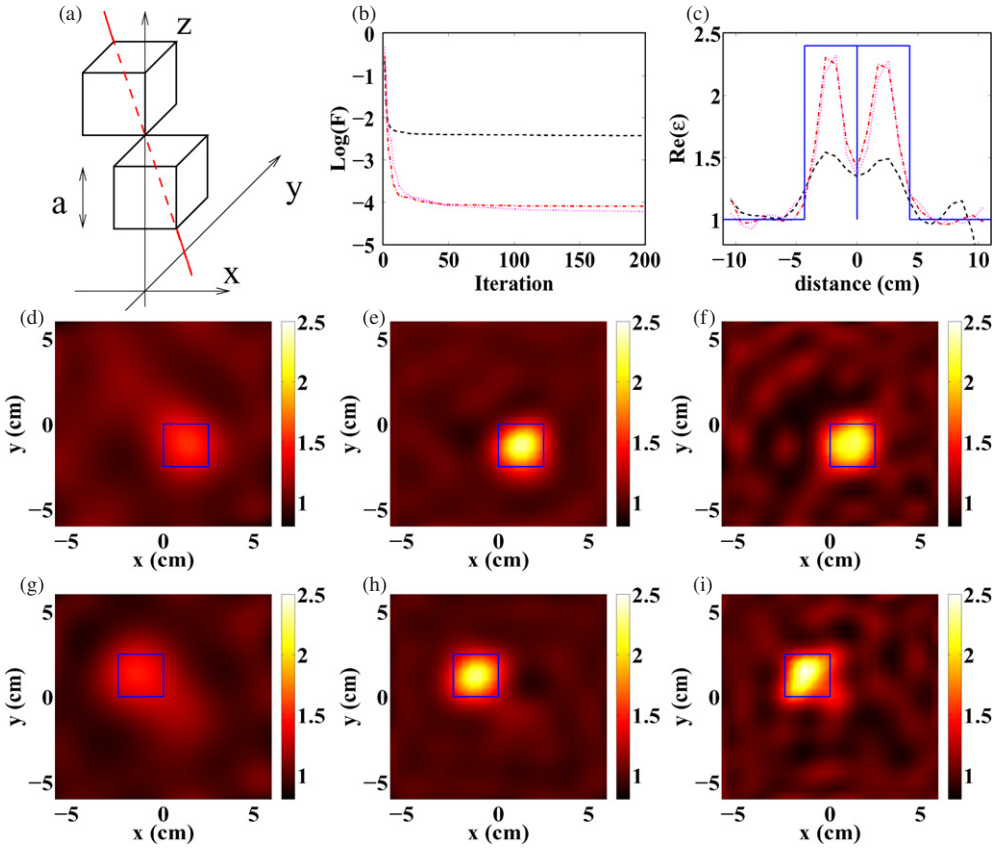

Figure 2. Same legend as in figure 1.

presented results the initial estimate α_0 to start the iterative process is obtained, thanks to the back-propagation procedure as described in [7].

The measure has been done for two polarizations of the emitting antenna and only one for the receiving antenna. Data were saved in separate files. We merged the two files and applied the reciprocity theorem, i.e. switched the role of the emitter and the receiver. Doing so, we end up with a single polarization of the excitation (the incident field, modeled as a plane wave, is polarized along the z-axis) and three components of the scattered field.

The numerical computation of the inversion algorithm takes about 10 h, on a computer of a clock frequency of 3 GHz, to invert one set of the database, i.e. one target at a single operating frequency. The main time of the computation is spent to solve equation (1). At the first iteration step, it takes only 1 min to solve the linear system for all angles of incidence while at the last iteration step the same operation takes about 3 min. The reduced computational time at the first iteration step is due to the fact that the initial guess provided by the back-propagation technique [7] corresponds to a weak scatterer for which the iterative computation of the internal electromagnetic field from equation (1) converges rapidly. Conversely, at the last iteration step, the object for which the computation of the internal field is performed is of a higher value of relative permittivity. It is possible to drastically reduce this computational time by using an extrapolation procedure to generate an efficient initial guess for the field

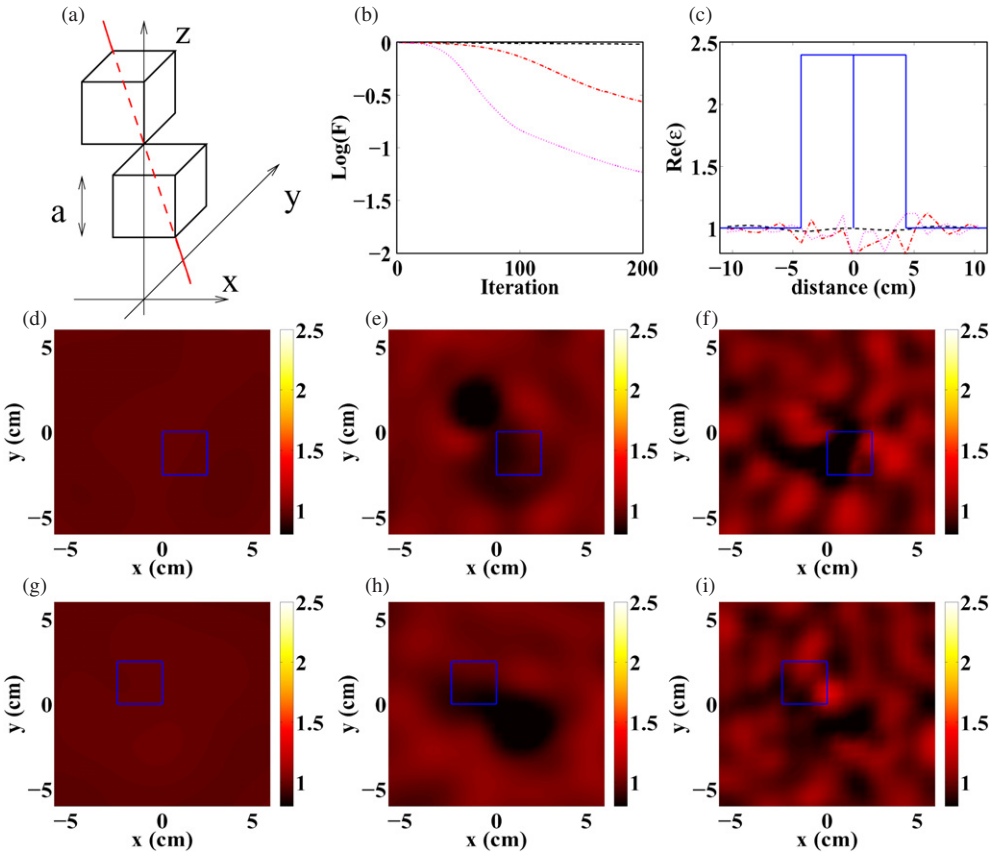

Figure 3. Same legend as in figure 1.

[37, 38]. The other operations, i.e. the computation of the cost function, the updating directions which involve gradients of the cost functional with respect to the parameter of interest, etc, take only 15 s.

4.1. Two identical cubes

As a first example, we consider the target constituted by two dielectric cubes of relative permittivity $\varepsilon = 2.4$ and of side size $a = 2.5$ cm connected by a corner as depicted in figure 1(a). Inversions have been performed at three frequencies of 3, 5 and 7 GHz. Reconstructed profiles are plotted in figures 1(d)–(i) while the evolution of the minimized cost function in log-scale versus iteration step is presented in figure 1(b). Figure 1(c) presents the comparison between the actual permittivity profile and the reconstructed ones along a line crossing the diagonals of the two cubes as well as the shared corner of the two cubes. Figures 1(d)–(f) represent the reconstructed permittivity in the (x, y) plane at $z = 3a/2$ (center of one of the two cubes) for frequencies of 3, 5 and 7 GHz, respectively. Figures 1(g)–(i) also represent reconstructed permittivity in the (x, y) plane for frequencies of 3, 5 and 7 GHz, respectively, but at different z positions ($z = 5a/2$ which corresponds to the center of the second cube).

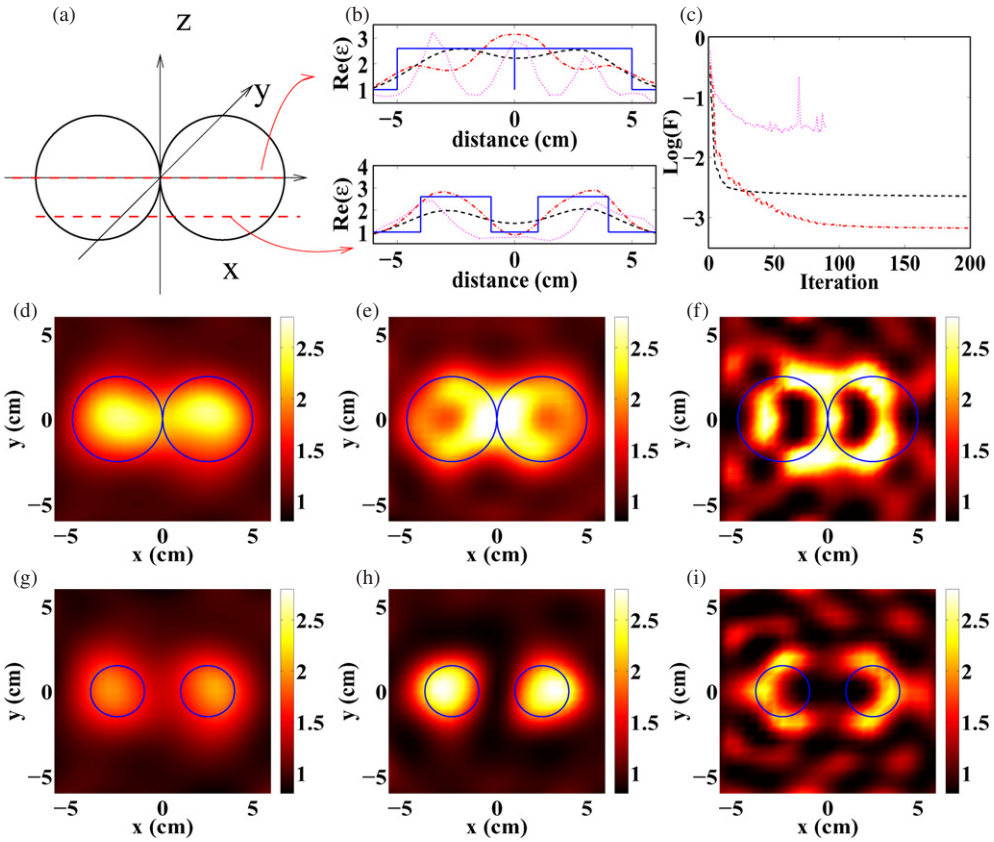

Figure 4. (a) Target under test: two spheres in contact with relative permittivity $\varepsilon = 2.6$ and of radius $r = 2.5$ cm. Centers of spheres are located at $(-r, 0, 0)$ and $(r, 0, 0)$. (b) Comparison between the reconstructed permittivity and the actual one along the x-axis for 3 GHz (- -), 4 GHz (-·) and 6 GHz (· · ·) (for $y = z = 0$ (up) and for $y = 0, z = -2$ cm (down)). The full line represents the actual profile. (c) Evolution of the minimized cost function in the log scale for 3 GHz (- -), 4 GHz (-·) and 6 GHz (· · ·). (d)–(f) are the map of the reconstructed relative permittivity in the (x, y) plane at $z = 0$ for 3 GHz, 4 GHz and 6 GHz, respectively. (g)–(i) as the previous figures but for $z = -2$ cm. Circles represent boundaries of the spheres.

At the lowest frequency, i.e. 3 GHz, the resolution of the reconstructed permittivity is 'poor'. Indeed, figures 1(d) and (g) show that neither the relative permittivity nor the shape of the two cubes are correctly retrieved. This is emphasized in figure 1(c) where quantitative comparison between the actual and reconstructed profiles is presented. This is not surprising as the wavelength of illumination is about $\lambda \approx 10$ cm while the characteristic dimension of the cubes is $a = 2.5$ cm $\approx \lambda/4$. Increasing the frequency up to 5 GHz, the reconstructed permittivity gets closer to the actual one (see figure 1(c)) and the reconstructed cubes plotted in figures 1(e) and (h) are now centered at the right positions. However, the shape of the cubes is still not well retrieved. For the inversion at 7 GHz, one can note in figures 1(f) and (i) that the retrieved shape clearly improved and now fits the actual shape.

We have also applied our inversion algorithm to retrieve the target from only one polarization data. Figure 2 presents results in the case where only the co-polarization data are used. Maps of reconstructed relative permittivities (figures 2(d)–(i)) are similar to those

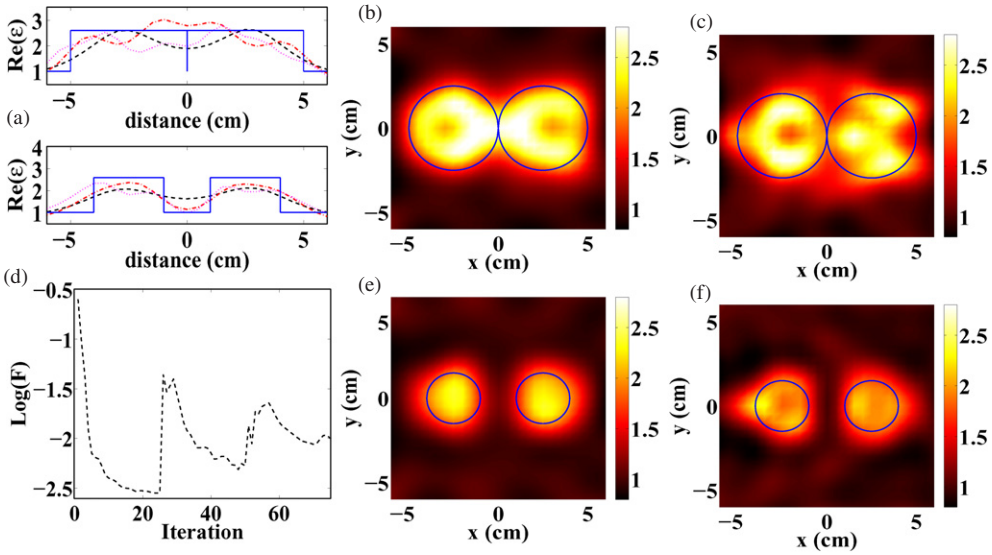

Figure 5. (a) Comparison between the reconstructed real part of the relative permittivity and the actual one along the x-axis for 4 GHz (- -), 5 GHz (-·) and 6 GHz (· · ·) (for $y = z = 0$ (up) and for $y = 0, z = -2$ cm (down)). The full line represents the actual profile. (d) Evolution of the minimized cost function in the log scale for 3 GHz (iteration 1–25), 5 GHz (iteration 26–50) and 6 GHz (iteration 51–75). (b) and (c) are the reconstructed relative permittivity distribution plotted in the (x, y) plane at $z = 0$ for 5 GHz and 6 GHz, respectively. (e) and (f) as the previous figures but for $z = -2$ cm. Circles represent boundaries of the spheres.

Table 1. Relative error in per cent between the scattered field given by the experiment and the scattered field computed theoretically from the actual shape.

Frequency	Co-polarization (%)	Cross-polarization (%)
3 GHz	14	94
5 GHz	5	56
7 GHz	8	44

obtained in the case where the inversion is performed using the full vectorial scattered field. This may be due to the fact that the two cubes do not depolarize the incident field.

Figure 3 presents the results of the inversion in the case where only the cross-polarization data are used. In this case, it is clear that the unknown object is not retrieved. Note that at the operating frequency of 7 GHz, the imaginary part is between -1 and 1. In order to understand the failure of the retrieval of the target, we compared the measured scattered field to the scattered field provided by the forward solver using the actual target. From this comparison, we observe that the co-polarization data are accurately measured and that the cross-polarization data are extremely noisy. This assumption is emphasized in table 1 where the relative error (L_2 norm) between the measured scattered and the computed one is reported.

The relative error corresponding to the cross-polarization data is high and is, for instance, close to 100% at 3 GHz. With such a high level of noise in the data, it is not possible to retrieve any information with respect to the target. Moreover, one can note that the relative error decreases for the cross-polarization data as the operating frequency increases. In fact

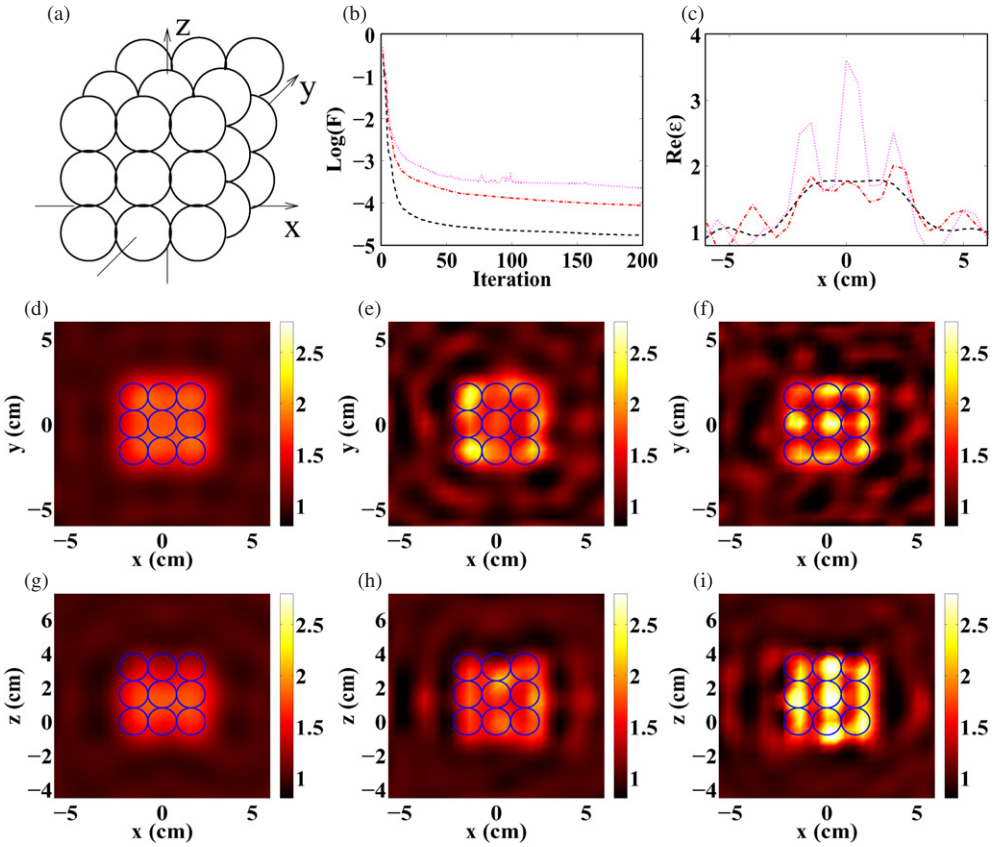

Figure 6. (a) Target under test: 27 spheres of radius $a = 0.795$ cm with relative permittivity $\varepsilon = 2.6$. The 27 spheres are arranged such that they form a cube. The location of the center sphere at the center of the cube is $(0, 0, 2a)$ cm. (b) Evolution of the minimized cost function in the log scale, 6 GHz (- -), 7 GHz (-·) and 8 GHz. (c) Relative permittivity versus x for $y = 0$ cm and $z = 2a$ for 6 GHz (- -), 7 GHz (-·) and 8 GHz ($\cdots$). (d)–(f) are the map of the reconstructed relative permittivity in the (x, y) plane at $z = 2a$ for 6 GHz, 7 GHz and 8 GHz, respectively. (g)–(i) are the map of relative permittivity plotted in the (x, z) plane at $y = 0$ cm for 6 GHz, 7 GHz and 7 GHz, respectively. Circles represent boundaries of the spheres.

as the frequency increases, the size of the object in terms of wavelengths increases as well; hence, the scattering magnitude increases. We guess that from the experimental point of view, it is easier to measure signals with high magnitude than signals of low magnitude.

4.2. Two identical spheres in contact

In this subsection, results of the reconstruction of two identical spheres in contact as shown in figure 4(a) are presented. The radius of each sphere is $r = 2.5$ cm and of relative permittivity $\varepsilon = 2.6$. Our inversion scheme, at the frequency of 3 GHz, provides a reconstructed relative permittivity smaller than the actual one (figure 4(b)) and the shape of the reconstructed spheres does not clearly indicate that the target under test is spherical. However, the reconstructed permittivity is much larger than that obtained for the two cubes. This is illustrated by figures 4(d) and (g) to be compared to figures 1(d) and (g). Significant improvements are

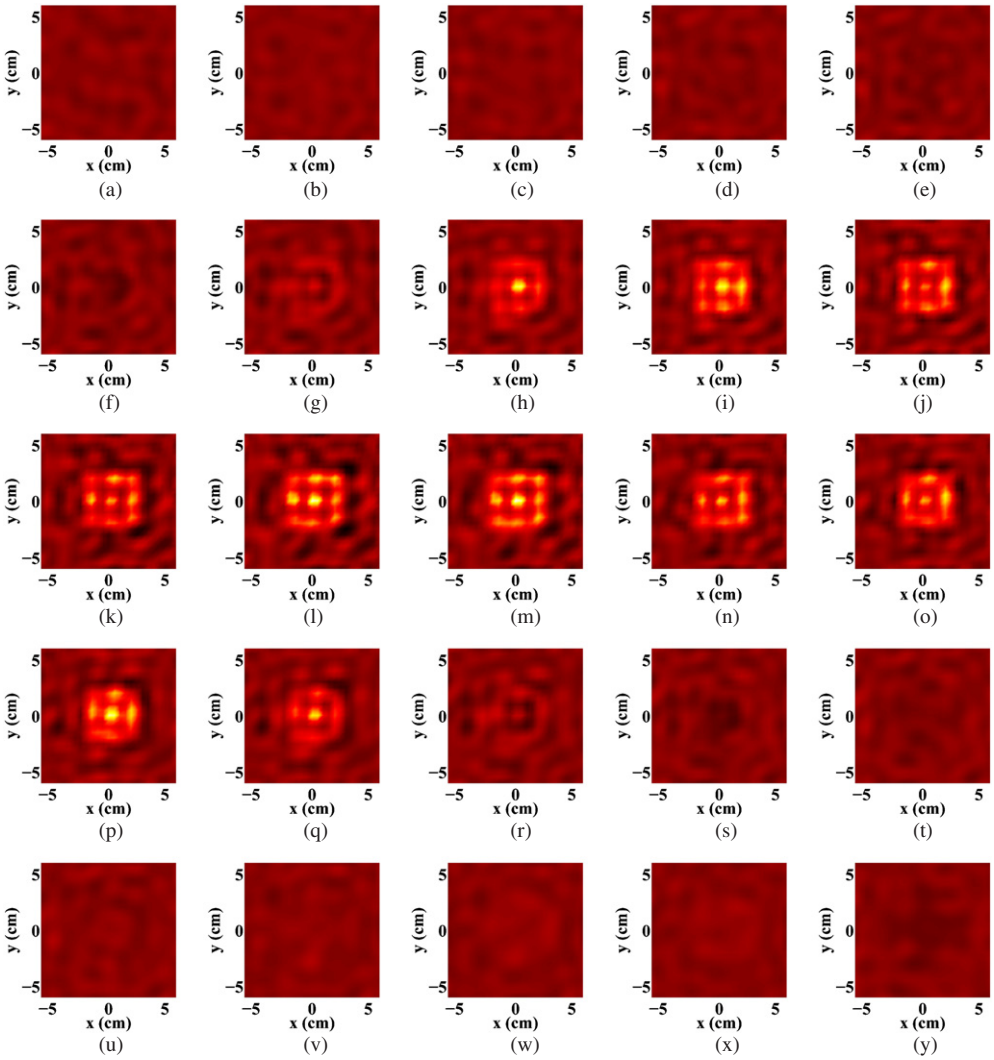

Figure 7. Reconstruction of the map of relative permittivity in the (x, y) plane for different values of z and for the frequency of 8 GHz. The inter-distance among the different planes is 5 mm. The color scale ranges from $\varepsilon = 0.5$ up to $\varepsilon = 3.6$.

obtained with the inversion at 4 GHz as presented in figures 4(e) and (h). Comparisons between the reconstructed profile and the actual one along two parallel lines at $z = 0$ cm and $z = -2$ cm are presented in figures 4(b) (top curve and bottom curve). The reconstructed permittivity in the (x, y) plane at $z = 0$ cm, figure 4(e), shows that the relative permittivity increases dramatically in the area where the spheres are in contact. Inversion at the higher frequency of 6 GHz does not converge as showed by the cost function plotted in figure 4(c), and the map of the reconstructed relative permittivity presented in figures 4(f) and (i) corresponding to the lower value of the cost function is far from the actual profile. When the frequency hopping is applied, i.e. the final result obtained at 4 GHz after 25 iterations is used as an initial guess for the inversion at 5 GHz, the reconstruction presented in

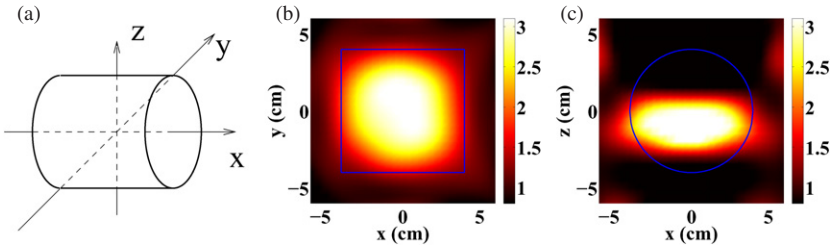

Figure 8. (a) Target under test: cylinder of radius $a = 4$ cm, length $2a$ with relative permittivity $\varepsilon = 3.05$. (b) Map of the reconstructed relative permittivity in the (x, y) plane at $z = 0$ cm. (c) Map of the reconstructed relative permittivity in the (x, z) plane at $y = 0$ cm. The square in (b) and the circle in (c) represent the boundaries of the cylinder.

figures 5(a), (b) and (e) show that the two spheres are now perfectly retrieved. The reconstruction is improved drastically when pursuing the frequency hopping approach, i.e. when the final result obtained at 5 GHz after 25 iterations is used as an initial guess for the inversion at 6 GHz as illustrated in figures 5(a), (c) and (f) to be compared to figures 4(f) and (i).

4.3. Aggregate of 27 spheres

The object under study in this subsection is as depicted in figure 6(a). It is constituted of an aggregate of 27 spheres of relative permittivity $\varepsilon = 2.6$ and of radius $a = 0.795$ cm. Inversions have been performed at three frequencies of 6, 7 and 8 GHz. The evolution of the minimized cost function in the log scale versus iteration step is presented in figure 6(b). Figure 6(c) presents the reconstructed profile along the x-axis for $y = 0$ cm and $z = 2a$. Figures 6(d)–(f) represent the reconstructed permittivity in the (x, y) plane at $z = 2a$ for frequencies of 6, 7 and 8 GHz, respectively. Figures 6(g)–(i) also represent reconstructed permittivities, but in the (x, z) plane for $y = 0$ for frequencies of 6, 7 and 8 GHz, respectively.

At the frequency of 6 GHz, figures 6(d) and (g), the side size of the aggregate is about one wavelength while the size of the spheres is about $\lambda/3$. Due to the small size of the spheres compared to the wavelength, it is difficult to retrieve such small details. Hence, inversion at this frequency provides only a rough estimate of the target under test. The retrieved object looks like a homogeneous object of the same size as the size of the cube of the aggregate of the spheres and of relative permittivity smaller than that of the sphere. The underestimated value of the reconstructed relative permittivity may be explained as a compensation to the large retrieved volume. Results of inversions at higher frequency, 7 GHz and 8 GHz, show as expected the details. The map of the reconstructed relative permittivity at 8 GHz in the (x, y) plane is presented in figure 6(f). The spheres are now clearly distinguished. The improvement of the resolution is obviously related to the decrease of the wavelength of illumination. Note that the map of relative permittivity in the (x, z) plane, figure 6(i), shows that the sphere is not retrieved along the z-axis. This is due to the reduction by a factor of 2 of the Ewald sphere in the z-direction compared to the Ewald sphere in the x-direction.

Figure 7 presents the results of our inversion at the frequency of 8 GHz in the entire investigating domain Ω. Figures 7(j) and (p) represent the reconstructed relative permittivity distribution in the first and the third layers of the assembly of the spheres, respectively. It shows that the spheres located at the corner of the cube appear with a relative permittivity

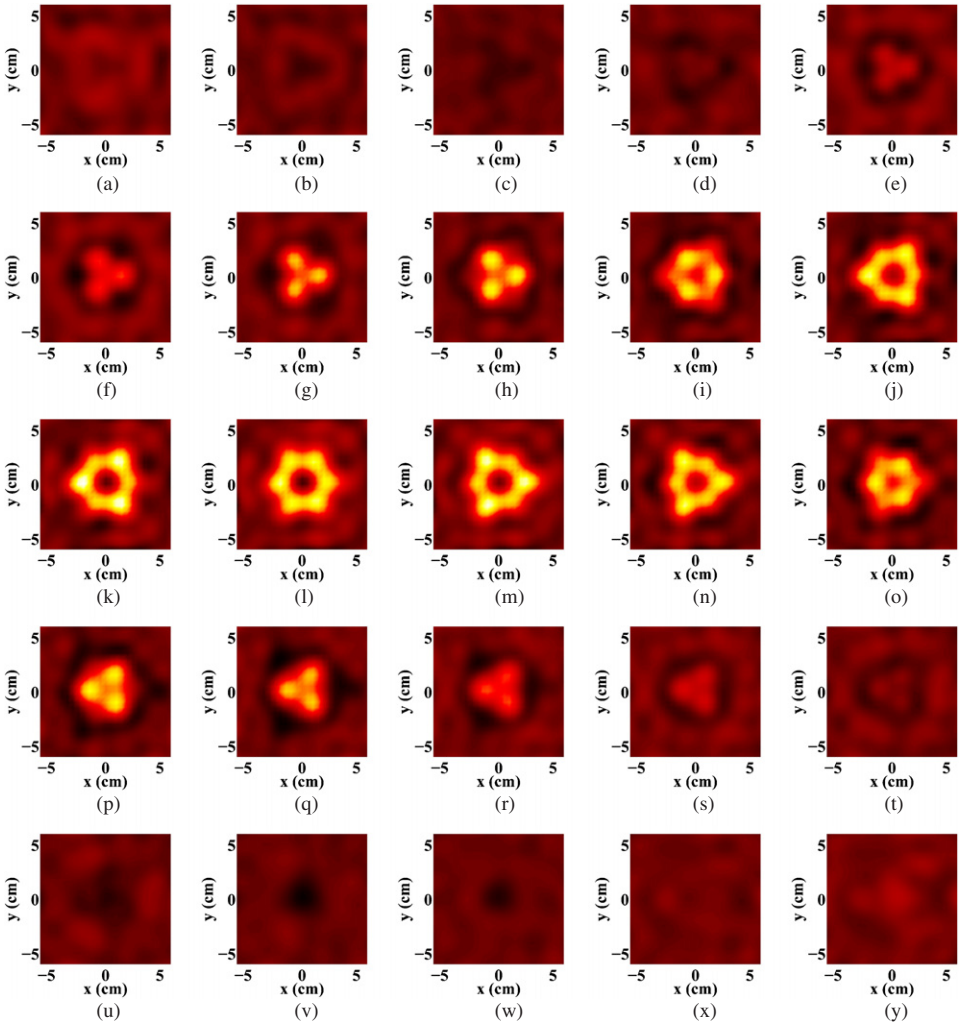

Figure 9. Reconstruction of the map of relative permittivity in the (x, y) plane for different values of z and for the frequency of 6 GHz. The inter-distance among the different planes is 5 mm. The color scale ranges from $\varepsilon = 0.8$ up to $\varepsilon = 2.7$.

smaller than the other spheres. The sphere at the center of the cubes is retrieved with a higher relative permittivity (3.6).

4.4. Cylinder

In this subsection, results of the reconstruction of a cylinder of radius $a = 4$ cm, of length $2a$ and of relative permittivity $\varepsilon = 3.05$ (figure 8(a)) are presented. We present only the results of our inversion at the frequency of 3 GHz and for the 13th iteration step. The cost function increases dramatically. At the 19th iteration, the retrieved relative permittivity is between $[-100; 80]$ and the cost function is above 10^{18}. Such behavior of the inversion indicates that for this case, the inversion diverged. For the other frequencies, our inversion scheme fails to

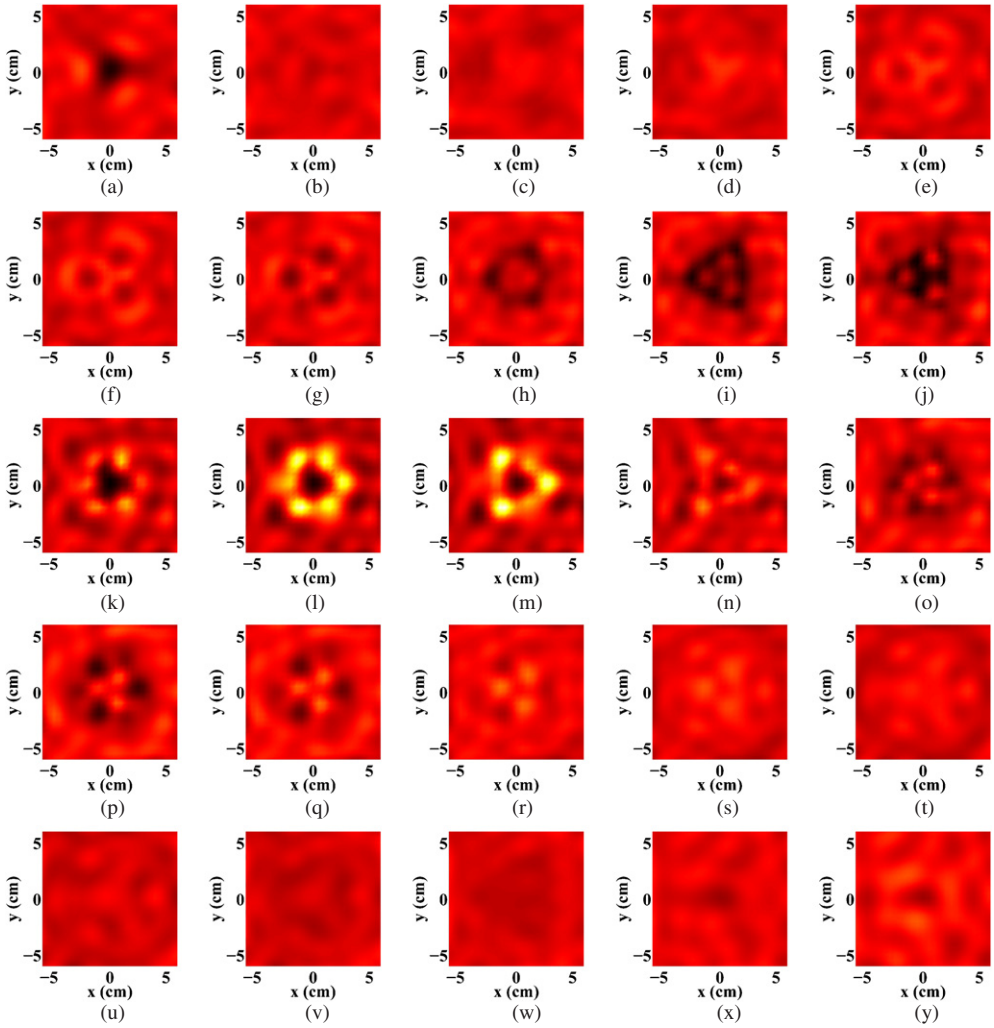

Figure 10. As in figure 9 but for the imaginary part of the relative permittivity. The color scale ranges from $\mathrm{Im}(\varepsilon) = -0.3$ up to $\mathrm{Im}(\varepsilon) = 0.6$.

retrieve the cylinder as well. This is due to the high value of the actual relative permittivity correlated with the large size of the cylinder compared to the wavelength of illumination. Indeed, at the frequency of 4 GHz the size of the cylinder is twice the wavelength inside the cylinder. Our method as described in the present paper is not capable of retrieving such strong targets. For these cases, regularization techniques and/or *a priori* information are mandatory.

Notwithstanding the difficulty of reconstructing strong targets, we were however able to obtain some information regarding the position of the cylinder. Figures 8(a) and (b) present the map of relative permittivity in the (x, y) plane and (x, z) plane, respectively. One can note that the cylinder is correctly localized in the (x, y) plane with a relative permittivity of about 3 for the maximum value. But the retrieved shape does not fit properly the actual one. In the (x, y) plane, neither the localization nor the shape of the cylinder are properly retrieved.

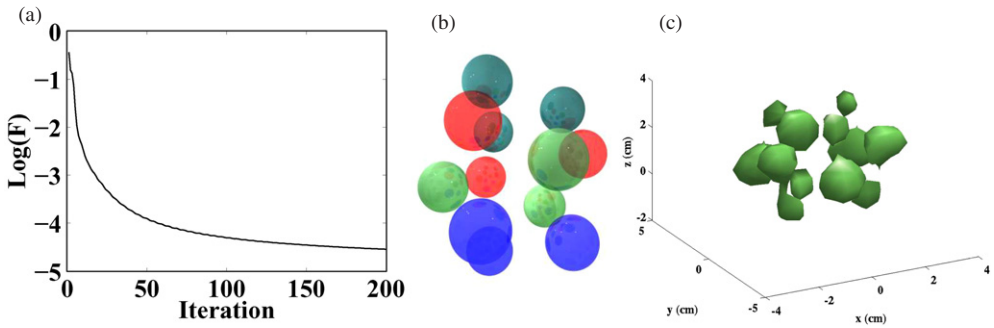

Figure 11. (a) Evolution of the minimized cost function in the log scale versus iteration step for 6 GHz. (b) Guess of the mysterious object, where each color has been assigned to a given value of z. (c) Shape given by an iso-surface of the reconstructed permittivity profile at the level $\varepsilon = 2.1$.

4.5. Mysterious object

The object under study for this subsection is unknown. Hence, in figure 9 we plot the map of the relative permittivity in the (x, y) planes for all values of z. Two successive planes are separated by the distance d which is the value of the spacing lattice used to grid the investigating domain Ω. From the observations of the different images, one can see different objects: plane 8 shows three spots which could be three spheres, as well as planes 11, 13 and 16. Hence, we can deduce that the mysterious object is constituted by 12 spheres. Note that plane 12 shows six spots. This might be seen as a plane containing the top of the three spheres located at plane 11 and the bottom of the three spheres of plane 13. In figure 10, the imaginary part of the relative permittivity is plotted. The highest reconstructed value is 0.6. This value leads to a skin depth much lager than the size of the object. One can conclude that the reconstructed object is purely dielectric.

In figure 11(a), the cost function is plotted. It shows a good behavior of the convergence of the algorithm. Figure 11(c) shows an iso-surface at a level of $\varepsilon = 2.1$. It reveals 12 spherical-shaped objects. Hence, in figure 11(b) we draft an idea of the mysterious object. We think that the object is constituted of 12 different spheres as shown in figure 11(b). The radius of each sphere is about 8 mm and of relative permittivity $\varepsilon = 2.6$. The 12 spheres are distributed in four different planes, and the three spheres in each plane are located at the top of an equilateral triangle.

5. Conclusion

In this paper, we have tested our inversion scheme against real data. We performed blind inversion and did not use any *a priori* information (relative permittivity is complex). Satisfactory results have been obtained due to the fact that our inversion is based on retrieval of the polarizability rather than the standard permittivity distribution combined with our choice of the initial guess which is deduced from the back-propagation procedure. For the two known targets treated in this paper, the proposed inversion algorithm succeed in retrieving the shape as well as the constitutive material of the targets under test. For the mysterious target, we provided information about the positions, shapes, and the constitutive materials.

Acknowledgments

The authors would like to thank Visual Numerics Inc. France who kindly put the software PV-WAVE at the disposal of the Institute. This software helped us to analyze the results as well as the data especially for the mysterious target. The authors would like to thank Anne Sentenac for many fruitful discussions and for her daily smile.

References

[1] Tijhuis A G 1989 Born-type reconstruction of material parameters of an inhomogeneous lossy dielectric slab from reflected-field data *Wave Motion* **11** 151–73
[2] Chew W C and Wang Y M 1990 Reconstruction of two-dimensional permittivity distribution using distorted Born iterative method *IEEE Trans. Med. Imaging* **9** 218–25
[3] Abubakar A and van den Berg P M 2002 The contrast source inversion method for location and shape reconstructions *Inverse Problems* **18** 495–510
[4] Yu C, Yuan M, Stang J, Bresslour E, George R T, Ybarra G A, Joines W T and Liu Q H 2008 Active microwave imaging: II. 3D system prototype and image reconstruction from experimental data *IEEE Trans. Microw. Theory Tech.* **56** 991–1000
[5] Sentenac A, Chaumet P C and Belkebir K 2006 Beyond the Rayleigh criterion: grating assisted far-field optical diffraction tomography *Phys. Rev. Lett.* **97** 243901
[6] Belkebir K, Chaumet P C and Sentenac A 2006 Influence of multiple scattering on three-dimensional imaging with optical diffraction tomography *J. Opt. Soc. Am.* A **23** 586–95
[7] Belkebir K, Chaumet P C and Sentenac A 2005 Superresolution in total internal reflection tomography *J. Opt. Soc. Am.* A **22** 1889–97
[8] Chaumet P C, Belkebir K and Sentenac A 2004 Superresolution of three-dimensional optical imaging by use of evanescent waves *Opt. Lett.* **29** 2740–2
[9] Chaumet P C, Belkebir K and Lencrerot R 2006 Three-dimensional optical imaging in layered media *Opt. Express* **14** 3415–26
[10] Belkebir K and Sentenac A 2003 High resolution optical diffraction microscopy *J. Opt. Soc. Am.* A **20** 1223–9
[11] Chaumet P C, Belkebir K and Sentenac A 2007 Numerical study of grating-assisted optical diffraction tomography *Phys. Rev.* A **76** 013814–7
[12] Destouches N, Guérin C A, Lequime M and Giovannini H 2001 Determination of the phase of the diffracted field in the optical domain. Application to the reconstruction of surface profiles *Opt. Commun.* **198** 233–9
[13] Lauer V 2002 New approach to optical diffraction tomography yielding a vector equation of diffraction tomography and a novel tomographic microscope *J. Microsc.* **205** 165–76
[14] Geffrin J-M, Chaumet P C, Eyraud C, Belkebir K and Sabouroux P 2008 Electromagnetic three-dimensional reconstruction of targets from free space experimental data *Appl. Phys. Lett.* **92** 194103
[15] Purcell E M and Pennypacker C R 1973 Scattering and absorption of light by nonspherical dielectric grains *Astrophys. J.* **186** 705–14
[16] Chaumet P C, Sentenac A and Rahmani A 2004 Coupled dipole method for scatterers with large permittivity *Phys. Rev.* E **70** 036606–6
[17] Kahnert F M 2003 Numerical methods in electromagnetic scattering theory *J. Quantum Spect. Rad. Transf.* **79–80** 775–824
[18] Yurkin M A and Hoekstra A G 2007 The discrete dipole approximation: An overview and recent developments *J. Quant. Spectrosc. Radiat. Transfer* **106** 558–89
[19] Jackson J D 1975 *Classical Electrodynamics* 2nd edn (New York: Wiley)
[20] Rahmani A, Chaumet P C, de Fornel F and Girard C 1997 Field propagator of a dressed junction: fluorescence lifetime calculations in a confined geometry *Phys. Rev.* A **56** 3245–54
[21] Rahmani A, Chaumet P C and Bryant G W 2004 On the importance of local-field corrections for polarizable particles on a finite lattice: application to the discrete dipole approximation *Astrophys. J.* **607** 873–8
[22] Rahmani A, Chaumet P C and Bryant G W 2002 Local-field correction for an interstitial impurity in a crystal *Opt. Lett.* **27** 430–2
[23] Dungey C E and Bohren C F 1991 Light scattering by nonspherical particles: a refinement to the coupled-dipole method *J. Opt. Soc. Am.* A **8** 81–7
[24] Draine B T and Goodman J 1993 Beyond Clausius–Mossotti: wave propagation on a polarizable point lattice and the discrete dipole approximation *Astrophys. J.* **405** 685–97

[25] Lakhtakia A 1992 Strong and weak forms of the method of moments and the coupled dipole method for scattering of time-harmonic electromagnetics fields *Int. J. Mod. Phys.* C **3** 583–603
[26] Lakhtakia A 1993 Errata on strong and weak forms of the method of moments and the coupled dipole method for scattering of time-harmonic electromagnetics fields *Int. J. Mod. Phys.* C **4** 721–2
[27] Chaumet P C 2004 Comment on 'Trapping force, force constant, and potential depths for dielectric spheres in the presence of spherical aberrations' *Appl. Opt.* **43** 1825–6
[28] Chaumet P C, Rahmani A and Nieto-Vesperinas M 2002 Selective nanomanipulation using optical forces *Phys. Rev.* B **66** 195405–11
[29] Chaumet P C, Rahmani A and Nieto-Vesperinas M 2005 Photonic force spectroscopy on metallic and absorbing nanoparticles *Phys. Rev.* B **71** 045425–7
[30] Chaumet P C, Rahmani A and Nieto-Vesperinas M 2006 Local-field enhancement in an optical force metallic nanotrap: application to single-molecule spectroscopy *Appl. Opt.* **45** 5185–90
[31] Nieto-Vesperinas M, Chaumet P C and Rahmani A 2004 Near-field photonic forces *Phil. Trans. R. Soc.* A **362** 719–37
[32] Draine B T 1988 The discrete-dipole approximation and its application to interstellar graphite grains *Astrophys. J.* **333** 848–72
[33] Freund R W and Nachtigal N M 1991 QMR—a quasi-minimal residual method for non-Hermitian linear-systems *Numer. Math.* **60** 315–39
[34] Goodman J J and Flatau P J 2002 Application of fast-Fourier-transform techniques to the discrete-dipole approximation *Opt. Lett.* **16** 1198–200
[35] Bordas F, Louvion N, Callard S, Chaumet P C and Rahmani A 2006 Coupled dipole method for radiation dynamics in finite photonic crystal structures *Phys. Rev.* E **73** 056601
[36] Chaumet P C, Rahmani A, Sentenac A and Bryant G W 2005 Efficient computation of optical forces with the coupled dipole method *Phys. Rev.* E **72** 046708–6
[37] Peng Z Q and Tijhuis A G 1993 Transient scattering by a lossy dielectric cylinder: marching-on-in-frequency approach *J. Electromagn. Waves Appl.* **7** 739–63
[38] Chaumet P C, Belkebir K and Rahmani A 2008 Coupled-dipole method in time domain *Opt. Express* 20157–65